Microstructural characterisation of nickel rich areas and their influence on endurance limit of sintered steel

Bernier, F.; Plamondon, P.; Baïlon, J.-P.; L'Espérance, G.

Publisher's version / Version de l'éditeur:
https://doi.org/10.1179/1743290111Y.0000000006
Powder Metallurgy, 54, 5, 2011-12-01

Microstructural characterisation of nickel rich areas and their influence on endurance limit of sintered steel

F. Bernier*[1], P. Plamondon[2], J.-P. Baïlon[2] and G. L'Espérance[2]

Nickel is an often used alloying element in powder metal steel to achieve high hardenability. However, when nickel is added, the slow diffusion rate between iron and nickel leads to the formation of nickel rich areas (NRAs). Two steel alloys were studied: a Fe–6·4Ni–0·7Mo–0·7C with standard sized nickel powder additions and a Fe–2·4Ni–0·7Mo–0·7C with a finer sized nickel powder. Microstructural characterisation of the parts revealed that sufficient hardenability was achieved for both materials, but that NRAs were observed when standard sized nickel is used. X-ray energy dispersive spectrometry and electron diffraction show that the NRAs are composed of martensite and austenite under rapid cooling conditions. Three-point bending fatigue tests were carried out on both alloys to evaluate the effect of these soft austenitic areas on the fatigue properties of powder metal steel parts. The analysis of the endurance limit results shows that NRAs are not a governing factor.

Keywords: Fine nickel, Steel, Austenite, Hardenability, Endurance limit

Introduction

In order for powder metal (PM) steels to replace wrought steels in high performance applications, high dynamic properties, particularly fatigue, must be reached while maintaining cost competitiveness. One method to achieve high performance PM steels at low cost is the use of sinter hardening steel blends.[1] These powder blends enable the formation of martensite during the cooling stage of the sintering process, thereby avoiding the need for heat treatment and the problems of distortion and oil retention associated with quenching.[1–3] Nickel additions are widely used in high performance PM steels applications, as Ni is known to increase hardenability,[4–8] and thus increase the volume fraction of hard constituents such as martensite and lower bainite. These harder constituents were shown to be beneficial to achieve high tensile and fatigue properties compared with softer phases like upper bainite and pearlite.[7–9] However, the addition of nickel powder into PM steel leads to inhomogeneous microstructures and the formation of nickel rich areas (NRAs).[7–10] The presence of NRAs is usually explained by the slow diffusion of nickel into iron.[7–9] However, a recent study indicates that their presence is due to a slow solid state diffusion of iron into nickel after a fast grain boundary diffusion of nickel into iron.[10] Phases present in the NRAs can range from soft austenite and ferrite to hard bainite and martensite depending mainly on the local nickel content and cooling rate.[8,10–15] Despite recent interest in the effect of NRAs on mechanical properties, there is still a lack of information on their exact nature. The complex combination of martensite, austenite and other microstructural constituents obtained under sinter hardening conditions needs further understanding.

In the last decade, many studies investigated the impact of those NRAs on the mechanical properties of PM steels, particularly fatigue.[12–18] The NRAs are present predominantly at the periphery of pores and at the border of the steel powder particles.[13,17,19] Since fatigue crack initiation usually occurs at/or near pores in PM steels, the presence of austenite in these regions could affect fatigue performance.[20–24] Indeed, an improvement in the endurance limit was observed by Unami *et al.*[25] for PM steels and by Richman and Landgraf[26] for high carbon wrought steels for larger amounts of retained austenite. They attributed this improvement to the high ductility of austenite and to its strain induced martensitic transformation, which both consume energy that cannot be used for the initiation of cracks. However, strain incompatibility between the soft austenite and the hard martensite can lead to crack initiation at interphase boundaries.[27,28] In addition, Deng *et al.*[29] conducted surface measurements of the crack growth rate through different microstructural constituents and showed that the crack growth rate was more than an order of magnitude higher in austenite than in bainite. The endurance limit of steels is governed by the initiation of microcracks and particularly by the propagation of microcracks into a main crack.[30] Hence, further understanding of the impact

[1]Powder Forming Group, Industrial Materials Institute of the National Research Council Canada, 75 De Mortagne Blvd., Boucherville J4B 6YA, Canada
[2]Materials Engineering, École Polytechnique de Montréal, 2900 Édouard-Montpetit Blvd., Montréal H3T 1J4, Canada

*Corresponding author, email fabrice.bernier@cnrc-nrc.gc.ca

Published by Maney on behalf of the Institute
Received 25 January 2011; accepted 16 April 2011
DOI 10.1179/1743290111Y.0000000006

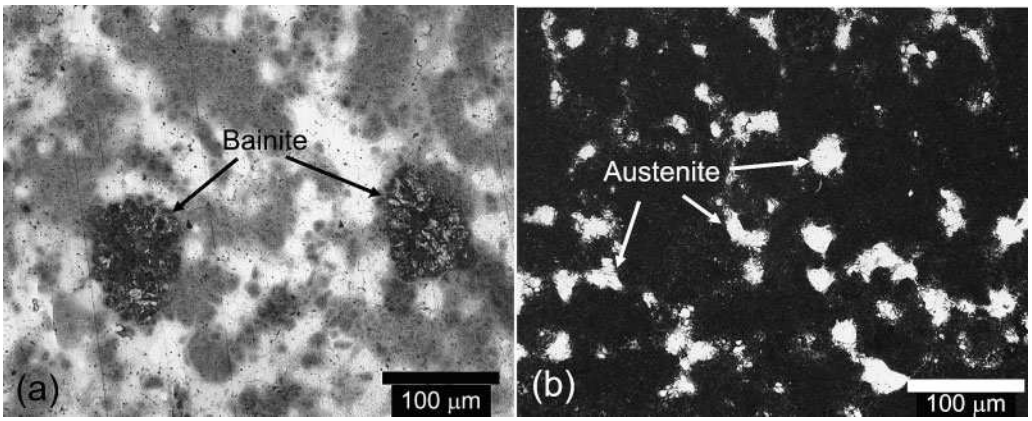

a etched with nital; *b* etched with nital-picral

1 Optical micrograph of Fe–6·4Ni–0·7Mo–0·7C alloy

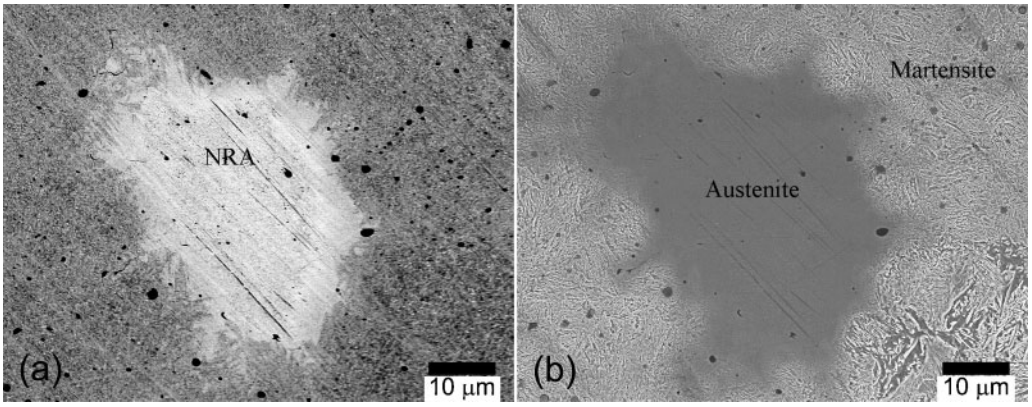

a as polished (backscattered electron imaging in SEM); *b* etched with nital–picral (secondary electron imaging in SEM)

2 Nickel rich areas in Fe–6·4Ni–0·7Mo–0·7C alloy

of those NRAs on the endurance limit of PM steels is needed.

The first part of this study was dedicated to examine the impact of the amount and the size of nickel powder additions on the microstructure. Optical microscopy in combination with etching techniques were used to quantify the different microstructural constituents obtained under sinter hardening conditions. Two PM steel mixes were studied. The first mix is Fe–2·4Ni–0·75Mo–0·7C where fine sized nickel powder was admixed to avoid the presence of NRAs while maintaining high hardenability. The second mix is Fe–6·4Ni–0·75Mo–0·7C, with standard sized nickel to achieve a large amount of NRAs. The nickel content of the NRAs was also characterised. Scanning electron microscopy (SEM) with X-ray energy dispersive spectrometry (EDS) were used to determine the overall composition of the NRAs. The influence of the local nickel concentration on the constituents formed was studied by transmission electron microscopy (TEM) using high spatial resolution X-ray EDS microanalysis in combination with electron diffraction.

The second part of this study focused on the fatigue properties of the two PM steel mixes. Special attention was paid to the influence of the NRAs on the endurance limit. Crack initiation was also investigated using SEM on interrupted fatigue specimens.

Table 1 Volume fraction of microstructural constituents

Alloy	Martensite	Austenite	Bainite
Fe–2·4Ni–0·7Mo–0·7C	91	$\leqslant$0·5	8·5$\pm$1·2
Fe–6·4Ni–0·7Mo–0·7C	89·2	5·9$\pm$1·3	4·9$\pm$1·0

Experimental

The PM alloys studied were prepared using a prealloyed base powder (Domfer), containing nickel and molybdenum; the composition of the steel powder is Fe–0·005C–0·32O–0·028S–0·41Mn–0·74Mo–0·44Ni (wt-%). Two PM blends were prepared by adding 6 wt-% of standard sized nickel (d_{50}=7·5–8·5 μm; Vale Inco type 123) in one case and 2 wt-% of fine nickel (d_{50}=1–2 μm; Vale Inco type T110D) in the other case. Both blends were also admixed

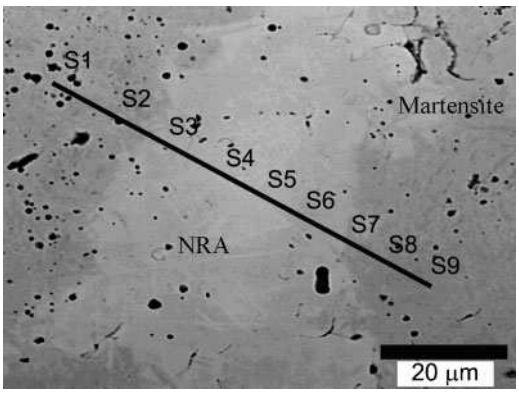

3 Secondary electron SEM of NRA in Fe–6·4Ni–0·7Mo–0·7C alloy and position of EDS analysis (as polished)

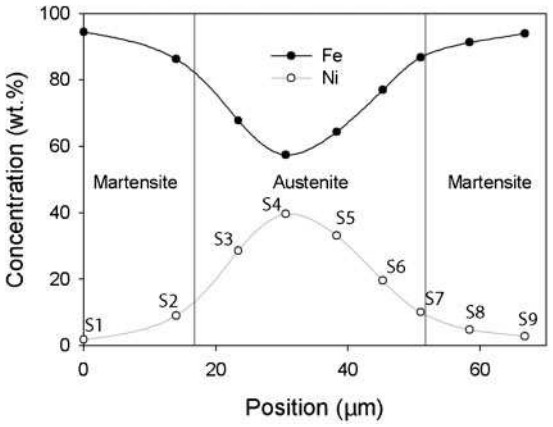

4 Energy dispersive spectrometry line profile in SEM of NRA shown in Fig. 3

with 0·85 wt-% graphite and 0·75 wt-% lubricant (zinc stearate). Specimens were then prepared by double press double sinter. Rectangular specimens ($31{\cdot}8 \times 12{\cdot}7 \times 6{\cdot}4$ mm) were initially pressed at 800 MPa and presintered at 800°C for 30 min in nitrogen. They were then pressed a second time to achieve a sintered density of 7·2 g cm^{-3}. The specimens were finally sintered at 1120°C for 30 min in nitrogen and rapidly cooled using a nitrogen gas stream to achieve a cooling rate between 1·5 and 2·5°C s^{-1} in the temperature range from 550 to 350°C. All specimens were tempered at 390°C for 1 h. This upper range of tempering temperatures was used to regain a high amount of ductility.[8] Sintering and heat treatment were carried out in a lab scale tubular type furnace.

Metallographic specimens were examined by optical microscopy and SEM (JEOL-JSM 7600F) in the etched condition to characterise the different phases present. Microhardness (Buehler Micromet II) values were also obtained to confirm the phase identification from the metallographic observations. The volume fraction of the microstructural constituents was quantified by optical microscopy in the etched conditions with an automated image analysis system (Clemex Vision PE). Quantitative X-ray EDS analysis was performed in the SEM using pure Fe, Ni and Mo as calibration standards at a beam energy of 15 keV. Standard quantification techniques were used.[31] The ratios of the sample intensity and the standard intensity, after continuum background was substracted, were first obtained. Then a matrix correction for atomic number, absorption and fluorescence (ZAF factor) was applied to quantify each element.

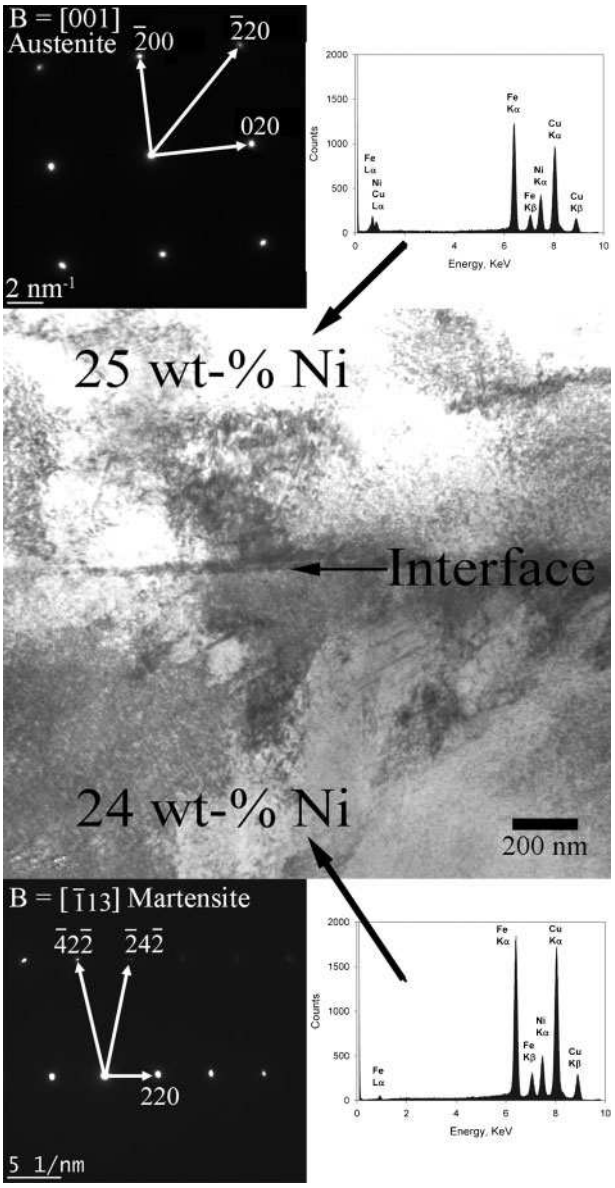

5 Image (TEM) of interface between austenite and martensite in Fe–6·4Ni–0·7Mo–0·7C alloy with corresponding diffraction patterns and EDS spectra

Electron diffraction in TEM (JEOL 2100F operated at 200 kV) was also used to determine the phases present in the NRAs and their composition was quantified by standardless EDS. The SEM was also used on interrupted fatigue specimens for crack initiation analysis.

Table 2 Quantitative X-ray EDS analysis in SEM for Fe–6·4Ni–0·7Mo–0·7C alloy*

		Nickel		Iron		Molybdenum	
Site	Position/μm	Intensity ratio	wt-%	Intensity ratio	wt-%	Intensity ratio	wt-%
S1	0	1·8	1·9	94·6	94·4	0·7	0·9
S2	14·0	8·6	9·1	87·1	86·3	0·7	0·9
S3	23·4	27·6	28·6	69·9	67·8	0·4	0·6
S4	30·6	38·5	39·7	60·1	57·4	0·3	0·4
S5	38·3	32·1	33·2	66·7	64·4	0·3	0·4
S6	45·3	18·9	19·6	78·6	77·0	0·5	0·7
S7	51·0	9·7	10·1	97·6	86·8	0·7	0·8
S8	58·4	4·6	4·8	91·7	91·3	0·7	0·9
S9	66·8	2·7	2·9	94·4	94·0	0·7	0·9

*See Fig. 3 for the detailed position of the EDS analysis.

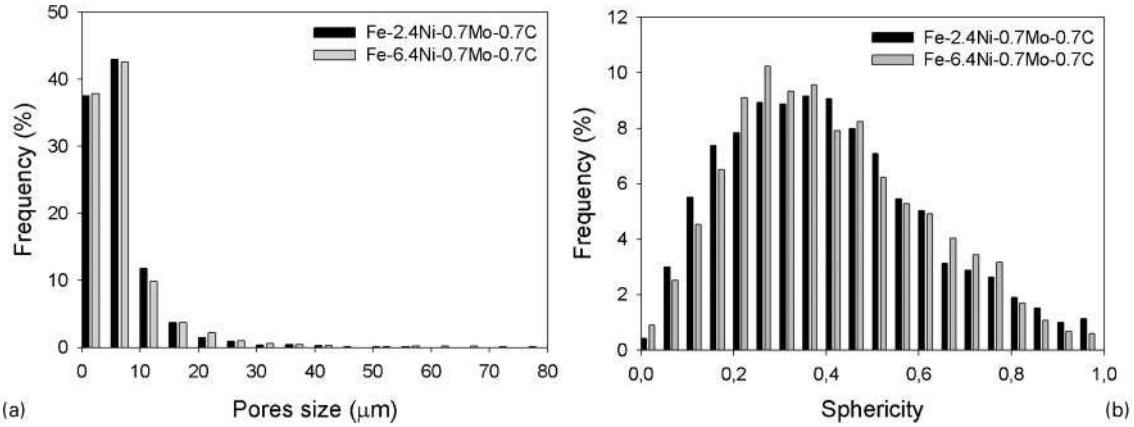

a size distribution; *b* morphology distribution

6 Pores characteristics

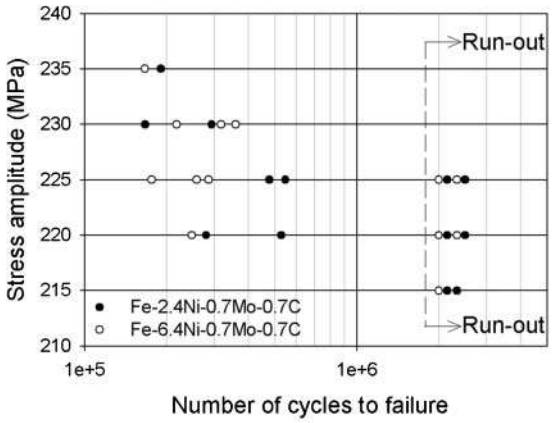

7 *S–N* curves of both alloys tested at *R*=0·1 in sinter hardened and tempered condition

These specimens were carefully polished with a 0·05 μm diamond suspension and then lightly etched.

Fatigue tests on the rectangular specimens were carried out using a load control fatigue machine (Instron) with a three-point bending apparatus operated at a frequency of 20 Hz and a R ratio ($\sigma_{min}/\sigma_{max}$) of 0·1. Fatigue specimens were hand polished with a diamond paste to a 1 μm finish. The staircase method was used to determine the endurance limit, using a 2 million cycles runout limit. This method, described by Weibull,[32] consists in submitting specimens for fatigue tests at different stress levels near the estimated endurance limit. If failure of a specimen occurs at a stress level x, the next test will be conducted at a stress level $x-d$, and on the contrary if there is no rupture (runout), the test will be done at $x+d$, where d is a fixed interval that should be lower than 10% of the endurance limit.[33] In our case, d was chosen to be under 5% to increase test resolution. The different stress levels are given a coded score i, where $i=0$ for the lowest stress level; also n_i refers to the number of failures (or runouts) at a given stress level. Two test parameters can then be calculated

$$A=\sum in_i \tag{1}$$

$$B=\sum in_i^2 \tag{2}$$

The endurance limit in terms of 50% survival σ_{50} and standard deviation s are calculated using only the total number of failures or the total number of runouts, depending on which of the two is the smallest

$$\sigma_{50}=\sigma_0+d\left(\frac{A}{\sum n}\pm\frac{1}{2}\right) \tag{3}$$

$$s=1{\cdot}62d\left(\frac{B\sum n-A^2}{(\sum n)}+0{\cdot}29\right) \tag{4}$$

where σ_0 is the lower stress level, Σn is the sum of all failures or runouts and in equation (3), '+½' is used if the number of runouts is more frequent and '−½' if the number of failures is more frequent. Finally, the estimation of standard deviation is valid if and only if the following expression is satisfied

$$\frac{B\sum n-A^2}{(\sum n)^2}\geq 0{\cdot}3 \tag{5}$$

Hence, to achieve statistically reliable results, approximately 15 specimens of each alloy were tested.

Results

Microstructural characterisation

The volume fraction of the microstructural constituents obtained under sinter hardening conditions for both alloys was quantified by a two step image analysis on optical micrographs. First, the volume fraction of bainite was determined with a nital specimen etched (Fig. 1*a*). The bainite regions appear darker than the martensite/

Table 3 Apparent hardness and microhardness

Alloy	Apparent hardness/HRC	Microhardness/HV		
		Martensite (100 gf)	Austenite (25 gf)	Bainite (100 gf)
Fe–2·4Ni–0·7Mo–0·7C	33±2	508±42	…	299±31
Fe–6·4Ni–0·7Mo–0·7C	35±2	542±35	238±24	308±27

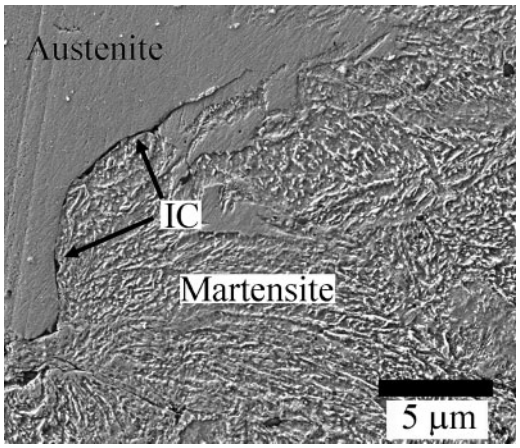

8 Interfacial cracking observed on runout sample of Fe–6·4Ni–0·7Mo–0·7C alloy at stress amplitude of 220 MPa

austenite regions. Then a nital–picral etch enables the quantification of the austenite which is revealed in bright white while the martensite and bainite are darkened (Fig. 1*b*). Finally, the volume fraction of martensite can then be calculated. The results of the microstructural quantification are presented in Table 1. These results show that nearly 90% of the volume fraction is martensitic for both alloys. Moreover, the alloy containing 6 wt-%Ni contains less bainite than the 2 wt-%Ni alloy. Bainite is replaced by the softer austenitic phase for the high nickel content alloy. Finally when fine sized nickel powder is used, NRAs are not observed.

A goal of this study was also to clearly identify and characterise the NRAs. First using backscattered electron imaging in the SEM, the NRAs appear brighter than the steel matrix due to the higher atomic number of nickel compared with that of iron (Fig. 2*a*). When the NRAs are etched with nital–picral, and observed using secondary electron images, the austenite remains light and smooth and the martensitic steel matrix is revealed (Fig. 2*b*). The size of the unetched austenite area is similar to that of the NRA observed with backscattered electron images.

Energy dispersive spectrometry quantitative analysis was performed to obtain the chemical composition of the NRA. Figure 3 shows the NRA where EDS analysis was made and the positions of different analysed spots. The results of the quantitative analysis are presented in Table 2. These results show a heterogeneous distribution of nickel in the NRA regions. The centre of the austenite phase has a lower molybdenum content, which indicates that this area was elemental nickel before it dissolved iron during sintering. From the centre of the austenite phase to the edge, the nickel content varies from 40 to 10 wt-% (Fig. 4). However, the exact composition at the interface of austenite and the martensite matrix cannot be obtained using EDS in the SEM because of contributions from the neighbouring region. Indeed, a Monte Carlo simulation based on the EDS parameters and on the composition of the alloys shows that the radius of the X-ray generation volume is ~0·8 μm. Therefore, to quantify with accuracy the nickel concentration at the interface between martensite and austenite, TEM was used. Indeed, TEM allows higher spatial resolution EDS analysis than SEM, since the radius of the X-ray generation volume is calculated to be about 11 nm in TEM compared to 0·8 mm in the SEM. Diffraction patterns were also obtained to clearly identify the microstructural constituents. Figure 5 is a TEM image of an interface, with the corresponding diffraction patterns and EDS spectra. The phase above the interface is austenite with a nickel composition of 25 wt-% while under the interface the phase is martensite with a composition of 24 wt-%. The copper peaks in the EDS spectrum are due to the copper grid. These results clearly indicate that for this mix cooled rapidly two types of nickel rich microstructural constituents are present: martensite with a nickel concentration under 25 wt-% and austenite when a nickel composition above 25 wt-%. This is in agreement with the constitutional diagrams for Ni steels.[11]

Finally, the fatigue properties of PM steels are strongly influenced by porosity. The size and shape of the pores and the stress concentration associated with them will affect the endurance limit. Indeed, microcracks usually originate from pores with the highest concentration factor.[14,19,20,24] Figure 6 compares the size and the shape factor distributions of the pores for the two alloys. Those results show that the pores are more irregular than spherical and that their major axis is mostly under 20 μm. In addition, since the results are similar for both alloys, the effect of the porosity can be neglected when comparing the endurance limit of the two alloys. It also appears that the size and amount of the nickel powder do not significantly affect the pore characteristics.

Mechanical properties

Apparent hardness and microhardness for the two alloys are described in Table 3. First, the apparent hardness is similar for both alloys even if their microstructural constituents differ. The microhardnesses of martensite and bainite are slightly larger for the high nickel content alloy. This difference is due to the higher nickel content in solution in the martensite and bainite constituents. The hardness of the martensite is comparable with that obtained for a quench and tempered (400°C for 1 h) eutectic wrought steel.[34] The results in Table 3 also show a large difference in hardness between the hard martensite and the soft austenite. The load used for the austenite regions was lower than that for martensite or bainite to ensure that the indentation does not impinge on other constituents.

The fatigue behaviour of the two alloys is illustrated in the stress versus cycle curves in Fig. 7 and Table 4 summarises the endurance limit in terms of 90, 50 and 10% survival. These results are similar for both alloys; hence their microstructural difference has no impact on the endurance limit. The presence of 6 vol.-% of austenite is not beneficial nor detrimental to the endurance limit of a PM steel containing 90% martensite. However, the observations of runout samples of the Fe–6·4Ni–0·7Mo–0·7C alloy show the presence of

Table 4 Endurance limit for both alloys, obtained by staircase method with runout limit of 2 million cycles

Alloy	Endurance limit/MPa			Standard deviation
	σ_{90}	σ_{50}	σ_{10}	
Fe–2·4Ni–0·7Mo–0·7C	211	223	234	8
Fe–6·4Ni–0·7Mo–0·7C	213	224	234	8

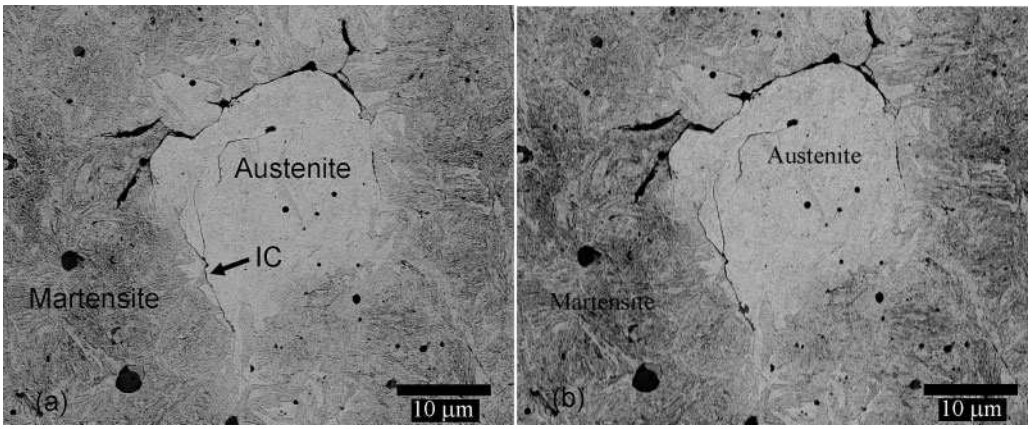

9 Microcrack at autenite/martensite interface observed in Fe–6·4Ni–0·7Mo–0·7C alloy fatigue sample interrupted after *a* 50 000 cycles and *b* 250 000 cycles

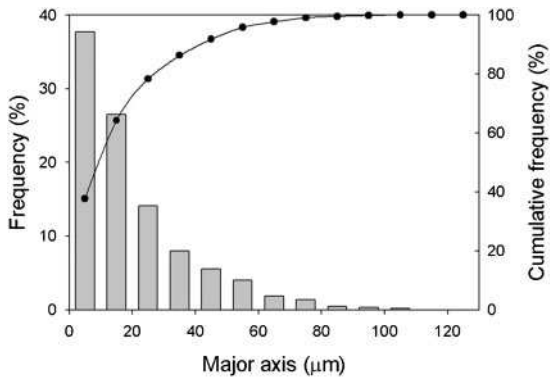

10 Distribution of major axis of austenite areas in Fe–6·4Ni–0·7Mo–0·7C alloy

microcracks (Fig. 8). These microcracks were present at the austenite/martensite interface and not inside the austenite area.

Discussion

The mechanism of fatigue fracture in steels has been extensively studied and consists of four events: nucleation of microcracks, propagation of microcracks, propagation of main crack(s) and final rupture. Figure 9 presents SEM images of a fatigue sample tested under a stress amplitude of 220 MPa interrupted after different cycles. Figure 9*a* shows austenite/martensite interfacial cracking early in the test life, after 50 thousands cycles. Indeed, the strain incompatibility between austenite and martensite leads to crack initiation, as observed elsewhere.[27,28] However, when the fatigue test is resumed and interrupted again after 250 thousands cycles, Fig. 9*b* shows that the microcrack did not propagate. This phenomenon was observed in many areas in the specimen and can be explained using fracture mechanics. Indeed, the stress intensity factor associated with a crack is given by the following equation

$$K = \alpha\sigma(\pi a)^{1/2} \tag{6}$$

where α is a parameter that depends on the specimen and crack geometry and a is the length of the crack. Under fatigue loading, the range of the stress intensity factor ΔK governs crack growth and is defined as

$$\Delta K = K_{\max} - K_{\min} \tag{7}$$

Hence by combining equations (6) and (7)

$$\Delta K = \alpha(\pi a)^{1/2}(\sigma_{\max} - \sigma_{\min}) \tag{8}$$

In our case, for a surface crack in an unotched three-point bending fatigue specimen, the value of α is between 1·0 and 1·1.[35] In addition, the value of the crack length due to interfacial cracking can be regarded as equivalent to the major axis of the austenitic area. Figure 10 shows the distribution of the major axis of the austenitic regions. Hence, the crack length should be under 40 μm at a cumulative frequency of 90%. For a stress amplitude of 220 MPa and a crack length of 40 μm, ΔK is equal to 5·4 MPa $m^{1/2}$. This value can be compared with the threshold value ΔK_{th}, below which cracks behave as non-propagating cracks. Carabajar *et al.* obtained a value for ΔK_{th} of 13·5 MPa $m^{1/2}$ at R=0·1 for a Fe–4Ni–1·5Cu–0·5Mo alloy with a similar microstructure but for a higher density of 7·4 g cm^{-3}.[13] The influence of density on ΔK_{th} is, however, small for a density range between 7·2 and 7·4 g cm^{-3}.[29] Hence, the ΔK associated with the microcracks originating from austenite/martensite interfacial cracking in our samples is considered to be well below the threshold value. Therefore, the austenite areas, even if their interface with martensite leads to crack initiation, are not a governing factor for the endurance limit of a Fe–6·4Ni–0·7Mo–0·7C PM steel. Indeed, the length of these interfacial cracks and the stress amplitude at the endurance limit lead to a range of the stress intensity factor below the threshold value of this material; hence these cracks does not propagate.

Conclusions

The microstructure and fatigue properties of two nickel containing PM steels pressed to a density of 7·2 g cm^{-3} were studied. The complete microstructural characterisation of a Fe–2·4Ni–0·75Mo–0·7C alloy where 2 wt-% fine sized nickel powder was admixed and a Fe–6·4Ni–0·75Mo–0·7C alloy where 6 wt-% standard nickel powder was admixed, shows that:

1. Both alloys are sinter hardenable; a cooling rate between 1·5 and 2·5°C s^{-1} leads to a martensite content of 90 vol.-%.

2. When 6 wt-% of standard sized nickel powder was added, the amount of austenite observed was 6 vol.-% of austenite, while NRAs were not observed when 2 wt-% fine sized nickel was added.

3. Nickel rich areas are a combination of austenite containing 25–40 wt-%Ni and martensite with a nickel content under 25 wt-%.

4. The higher amount of nickel in the mix containing 6 wt-% nickel increases the hardness of the martensite.

Three-point bending fatigue tests carried out on both PM alloys show that:

1. The endurance limit is similar for both alloys and the presence of 6 vol.-% of nickel rich austenite has no significant effect on the fatigue property.

2. Even if interfacial cracks between austenite and martensite were observed on interrupted and runout test specimens, the length of these cracks is too small to promote their propagation. The size of these cracks is related to the size of the austenitic areas.

Acknowledgements

This research was supported by the Natural Sciences and Engineering Research Council of Canada program Découvertes. One of the authors (FB) acknowledges the financial support of Auto21 (C202-PM: Powder Metallurgy for High-Performance Automotive Components) and École Polytechnique de Montréal.

References

1. H. Danninger and C. Gierl: *Int. J. Mater. Prod. Technol.*, 2007, **28**, 338–360.
2. S. N. Thakur, J. W. Newkirk, G. B. Fillari, T. F. Murphy and K. S. Narasimhan: *Int. J. Powder Metall.*, 2004, **40**, 45–54.
3. E. Duchesne, G. L'Esperance and A. de Rege: *Int. J. Powder Metall.*, 2000, **36**, 49–60.
4. B. Julien and G. L'Espérance: Proc. Conf. PM2TEC 1999, Vancouver, BC, Canada, June1999, MPIF, Vol. 7, 217–227.
5. S. Unami and S. Uenosono: Proc. Conf. PM2TEC 2003, Las Vegas, NV, USA, June 2003, MPIF, Vol. 5, 126–135.
6. T. Singh, T. F. Stephenson and S. T. Campbell: Proc. Conf. PM2TEC 2004, Chicago, IL, USA, June 2004, MPIF, Vol. 7, 93–104.
7. F. Bernier, P. Boilard, J.-P. Baïlon and G. L'Espérance: Proc. Conf. PM2TEC2005, Montréal, QC, Canada, June 2005, MPIF, Vol. 10, 201–210.
8. B. A. Gething, D. F. Heaney, D. A. Koss and T. J. Mueller: *Mater. Sci. Eng. A*, 2005, **A390**, 19–26.
9. S. Saritas, R. Causton, W. B. James and A. Lawley: *Int. J. Powder Metall.*, 2005, **41**, 63–70.
10. S. Sainz, W. Garcia, A. Karuppannagounder and F. Castro: *Powder Metall. Prog.*, 2007, **7**, 121–127.
11. F. W. Harbord: 'The metallurgy of steel'; 1911, London, Charles Griffin.
12. S. J. Polasik, J. J. Williams and N. Chawla: *Metall. Mater. Trans. A*, 2002, **33A**, 73–81.
13. S. Carabajar, C. Verdu and R. Fougeres: *Mater. Sci. Eng. A*, 1997, **A232**, 80–87.
14. N. Chawla, T. F. Murphy, K. S. Narasimhan, M. Koopman and K. K. Chawla: *Mater. Sci. Eng. A*, 2001, **A308**, 180–188.
15. M. W. Wu, K. S. Hwang and H. S. Huang: *Metall. Mater. Trans. A*, 2007, **38A**, 1598–1607.
16. S. Carabajar, C. Verdu, A. Hamel and R. Fougeres: *Mater. Sci. Eng. A*, 1998, **A257**, 225–234.
17. M. W. Wu and K. S. Hwang: *Metall. Mater. Trans. A*, 2006, **37A**, 3577–3585.
18. T. F. Stephenson and M. Gauthier: Proc. Conf. PowderMet2007, Denver, , CO, USA, May 2007, MPIF, Vol. 7, 288–298.
19. N. Chawla and X. Deng: *Mater. Sci. Eng. A*, 2005, **A390**, 98–112.
20. A. Hadrboletz and B. Weiss: *Int. Mater. Rev.*, 1997, **42**, 1–44.
21. H. Danninger, D. Spoljaric and B. Weiss: *Int. J. Powder Metall.*, 1997, **33**, 43–53.
22. A. Piotrowski and G. Biallas: *Powder Metall.*, 1998, **41**, 109–114.
23. E. A. Sager, R. I. Stephens and T. Prucher: *Powder Metall.*, 1998, **41**, 103–108.
24. H. Drar: *Mater. Charact.*, 2000, **45**, 211–220.
25. S. Unami, Y. Ozaki and S. Uenosono: Proc. Conf. PM2TEC 2003, Las Vegas, NV, USA, June 2003, MPIF, Vol. 7, 288–298.
26. R. H. Richman and R. W. Landgraf: *Metall. Trans. A*, 1975, **6A**, 955–964.
27. R. M. Ramage, K. V. Jata, G. J. Shiflet and E. A. Starke Jr: *Metall. Trans. A*, 1987, **18A**, 1291–1298.
28. Z. R. He, G. X. Lin and H. A. Chen: *Mater. Sci. Eng. A*, 2001, **A319**, 312–315.
29. X. Deng, G. Piotrowski, N. Chawla and K. S. Narasimhan: *Mater. Sci. Eng. A*, 2008, **A491**, 28–38.
30. Y.-L. Lee: 'Fatigue testing and analysis: theory and practice'; 2005, Burlington, MA, Elsevier Butterworth-Heinemann.
31. J. I. Goldstein and H. Yakowitz: 'Practical scanning electron microscopy: electron and ion microprobe analysis'; 1975, New York, Plenum Press.
32. W. Weibull: 'Fatigue testing and analysis of results'; 1961, New York, Pergamon Press.
33. C. Lipson and N. J. Sheth: 'Statistical design and analysis of engineering experiments'; 1973, New York, McGraw-Hill.
34. J.-P. Baïlon and J.-M. Dorlot: 'Des matériaux'; 2000, Montréal, Presses Internationales Polytechnique.
35. in 'ASM metal handbook', Vol. 19, 'Fatigue and fracture', 981–1000; 1996, Materials Park, OH, ASM International.